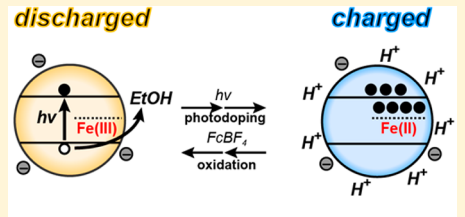
Downloaded via UNIV OF WASHINGTON on February 1, 2022 at 00:30:41 (UTC). See https://pubs.acs.org/sharingguidelines for options on how to legitimately share published articles.

Soluble Supercapacitors: Large and Reversible Charge Storage in Colloidal Iron-Doped ZnO Nanocrystals

Carl K. Brozek, † Dongming Zhou, † Hongbin Liu, † Xiaosong Li, † Kevin R. Kittilstved, † Dongming Zhou, and Daniel R. Gamelin*,†6

Supporting Information

ABSTRACT: Colloidal ZnO semiconductor nanocrystals have previously been shown to accumulate multiple delocalized conduction-band electrons under chemical, electrochemical, or photochemical reducing conditions, leading to emergent semimetallic characteristics such as quantum plasmon resonances and raising prospects for application in multielectron redox transformations. Here, we demonstrate a dramatic enhancement in the capacitance of colloidal ZnO nanocrystals through aliovalent Fe³⁺-doping. Very high areal and volumetric capacitances (33 μ F cm⁻², 233 F cm⁻³) are achieved in Zn_{0.99}Fe_{0.01}O nanocrystals that rival those of the best supercapacitors used in commercial energy-storage



250 e⁻ per Zn_{1-x}Fe_xO dot vs 50 e⁻ per ZnO dot

devices. The redox properties of these nanocrystals are probed by potentiometric titration and optical spectroscopy. These data indicate an equilibrium between electron localization by Fe³⁺ dopants and electron delocalization within the ZnO conduction band, allowing facile reversible charge storage and removal. As "soluble supercapacitors", colloidal iron-doped ZnO nanocrystals constitute a promising class of solution-processable electronic materials with large charge-storage capacity attractive for future energy-storage applications.

KEYWORDS: Supercapacitors, semiconductor nanocrystals, electronic doping, aliovalent doping

E lectron accumulation and depletion in colloidal semi-conductor nanocrystals (NCs) has been investigated as a means of turning on localized surface plasmon resonances and modulating their optical densities for redox sensing and electrochromic "smart" windows, for exploring interfacial electron transfer at the nanoscale, and for understanding fundamental aspects of quantum-confined multielectron configurations. $^{1-6}$ Photodoping has proven a convenient method for introducing excess electrons into colloidal semiconductor NCs.⁷⁻⁹ Promotion of valence-band electrons into the conduction band (CB) via photoexcitation, followed by rapid quenching of the photogenerated holes by sacrificial reductants, allows accumulation of multiple delocalized CB electrons (e^-_{CB}) per NC. Recently, we advanced these studies by demonstrating the use of spectroelectrochemical potentiometry to measure the effects of nanocrystal charge-carrier densities, surface compositions, electrolyte concentrations, and other factors on the NC redox potentials. 10-13 Using molecular oxidants to titrate these electrons, we showed that analysis of open-circuit potentials $(V_{\rm OC})$ plotted versus the average number of e^-_{CB} per NC $(\langle n \rangle)$ during potentiometric titration provides a direct measure of the capacitance of free-standing colloidal NCs.¹² Here, we report the observation of extremely large capacitance values from ZnO nanocrystals doped with redox-active iron impurities. Analysis shows that this high capacitance reflects the equilibrium between delocalized (band) and localized (impurity) levels within these NCs. The capacitance displayed by these colloidal NCs rivals those of

commercial supercapacitor materials, suggesting promising opportunities for application of these colloidal NCs in solution-based or solution-processed energy-storage technologies.

Our prior spectroscopic studies have indicated that colloidal Fe^{3+} -doped ZnO ($Zn_{1-x}Fe_xO$) NCs would be interesting candidates for potentiometric titration because of the accessibility of both oxidized (Fe³⁺) and reduced (Fe²⁺) impurity oxidation states under mild photodoping and aerobic oxidation conditions. 14,15 Fe3+-doped colloidal ZnO NCs were synthesized following the procedures we detailed previously. 14 For the samples investigated here, an average NC diameter of d = 8.7 nm is estimated from Scherrer analysis of their powder Xray diffraction (PXRD) data. Elemental analysis by inductively coupled plasma atomic emission spectroscopy (ICP-AES) indicates that Fe constitutes 1% of the lattice cations, giving an empirical formula of $Zn_{0.99}Fe_{0.01}O$ (neglecting any anion nonstoichiometry). Assuming spherical NCs, this composition corresponds to ~150 iron dopants per NC. For convenience, the NCs will be referred to here as Zn_{1-x}Fe_xO regardless of Fe oxidation state and cation/anion nonstoichiometry. Previous work^{8,16–18} has demonstrated that irradiation of colloidal ZnO and $Zn_{1-x}TM_xO$ (TM = Co^{2+} , Mn^{2+} , Fe^{3+}) NCs with UV light

Received: March 28, 2018 Revised: April 23, 2018 Published: April 25, 2018

Department of Chemistry, University of Washington, Seattle, Washington 98195-1700, United States

^{*}Department of Chemistry, University of Massachusetts, Amherst, Massachusetts 01003, United States

above the ZnO band gap in the presence of EtOH leads to accumulation of CB electrons, which causes a blue shift of the absorption edge and appearance of a broad new absorption band in the near-infrared, assigned as a localized surface plasmon resonance (LSPR). Figure 1A,B presents spectro-

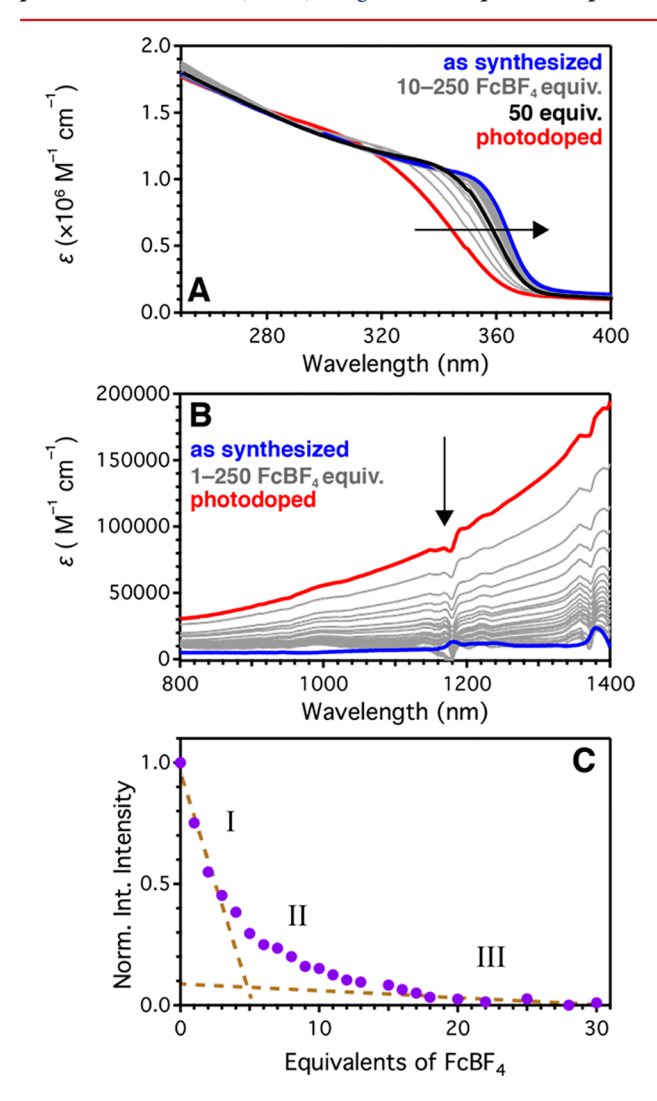


Figure 1. Absorption spectra of photodoped d=8.7 nm $Zn_{0.99}Fe_{0.01}O$ nanocrystals in THF titrated with $FcBF_4$ equivalents. (A) UV-visible absorption spectra of a 0.1- μ M NC solution plotted as molar extinction coefficient (ε). Titrants were added in 10 equivalent increments. (B) NIR absorption spectra of a 0.58 μ M NC solution. Titrants were added in 1 equivalent increments from 1–30 equiv and in 10 equivalent increments from 30–250 equiv. (C) Normalized NIR absorbance of $Zn_{0.99}Fe_{0.01}O$ NCs integrated between 800–1400 nm plotted versus equivalents of $FcBF_4$. Linear best-fits of titration equivalents 1–3 and 22–30 are shown as dashed lines. Three regimes are observed in the titration data, denoted by the labels I, II, and III.

scopic results collected before and after photodoping of the d = 8.7 nm $Zn_{0.99}Fe_{0.01}O$ NCs prepared here, confirming the bandedge (Figure 1A) and NIR (Figure 1B) spectral changes associated with electron accumulation.

Figure 1A,B also shows that these spectral changes are reversed upon addition of the outer-sphere one-electron oxidant $FcBF_4$ to remove e^-_{CB} equivalents. The data in Figure 1A show that a significant blue-shift of the absorption edge still remains after adding 50 $FcBF_4$ equivalents, and complete

recovery of the original absorption spectrum requires at least 250 oxidizing equivalents, i.e., $\langle n_{\rm max} \rangle \approx 250$. This value is confirmed by potentiometric titrations (*vide infra*).

Figure 1C summarizes the early titration data from Figure 1A,B by plotting the relative integrated NIR absorbance (800– 1400 nm) vs the number of FcBF4 equivalents added to maximally photodoped Zn_{0.99}Fe_{0.01}O NCs in the range of 0-30 oxidizing equivalents. Beyond 30 equiv, the NIR signal is too weak to be reliably quantified. In undoped ZnO NCs, the NIR absorption can be used to quantify $\langle n \rangle$ because of an approximately linear relationship between the two, but the data in Figure 1 show a strikingly nonlinear relationship. Instead, three distinct regimes (I, II, and III) are observed. Regime I (0-4 FcBF₄ equivalents) is approximately linear with a steep slope of -0.184 equiv⁻¹, indicating a large change in NIR absorption per electron. Regime III (15-30 FcBF₄ equivalents) is also approximately linear but with a much shallower slope of -0.002 equiv⁻¹. Regime II (5–15 equiv) bridges the other two regimes. These data support the presence of two distinct electron-storage reservoirs in these Zn_{1-x}Fe_xO NCs.

We interpret Regime I as involving changes in the e^-_{CB} population. The x-intercept of a best-fit line through the data in Regime I of Figure 1C provides a measure of the maximum average number of delocalized CB electrons per NC achieved via photodoping, which yields a value of $\langle n_{\text{max}}(CB) \rangle \approx 5$ for these Zn_{0.99}Fe_{0.01}O NCs. Regime III is interpreted as involving changes in Fe(3d) occupancy (Fe³⁺ \leftrightarrow Fe²⁺). The observation that oxidative titration effectively first depletes the ZnO NC CB and only subsequently depletes the Fe(3d) orbitals indicates an energetic difference (ΔE) between the CB edge and the midgap Fe(3d) orbitals. Specifically, these data indicate an Fe³⁺ + $e^$ binding energy that is sufficiently large to cause electron localization at iron. At the same time, however, the facile removal of electrons by outer-sphere oxidants in Regimes II and III also suggests that ΔE is sufficiently small so that the ZnO NC CB and Fe(3d) orbitals remain in redox equilibrium (eq 1).

$$Fe^{2+}:ZnO \rightleftharpoons e^{-}_{CB}, Fe^{3+}:ZnO$$
 (1)

Analysis of the data in Figure 1C provides an estimate of the equilibrium distribution of electrons between the ZnO NC CB and Fe(3d) orbitals, defined by the equilibrium constant in eq 2. For $K_{\text{eq}} = 0$, the concentration of CB electrons ($[e^{-}_{\text{CB}}]$) in Regime II would be zero, but instead the CB remains slightly populated because of some degree of Fe2+ ionization to generate e^-_{CB} . $[e^-_{CB}]$ can be quantified from the NIR absorbance beyond Regime I using the linear slope in Regime I, which describes the absorbance per e^-_{CB} . From $[e^-_{CB}]$ and the total number of Fe^{2+} ions per fully reduced NC (245), K_{eq} can be determined. After removing five electrons from the maximally photodoped Zn_{0.99}Fe_{0.01}O NCs (because $\langle n_{\text{max}}(\text{CB}) \rangle \approx 5$), [Fe³⁺] = [e^-_{CB}] and [Fe²⁺] = [245 - e^-_{CB}]. From Figure 1C, the NIR absorbance after removal of five electrons yields $[e^{-}_{CB}] = 1.25$. Solving eq 2 with these numbers yields $K_{eq} \approx$ 0.005 ± 0.003 . This estimate is subject to various sources of potential error, e.g., from the assumption of noninteracting electrons or from neglect of inhomogeneity within the NC ensemble. Nevertheless, different assumed parameters produce relatively little variation in $K_{\rm eq}$. Eq 3 transforms $K_{\rm eq}$ through the Nernst relationship to give $\Delta \hat{E} = 136$ mV, which is comparable to the binding energy estimated from variable-temperature deep-level transient spectroscopy measurements of bulk Fe-

doped ZnO (\sim 190 mV),¹⁹ lending credence to this analysis. Overall, this analysis indicates storage of \sim 245 excess electrons per NC in the Fe(3d) orbitals, compared to only about five electrons per NC in the ZnO CB. The charge-storage capacity of colloidal ZnO NCs has thus been increased by over an order of magnitude simply by 1% Fe doping. Interestingly, this capacity exceeds the maximum of 150 electrons expected from converting all Fe³⁺ dopants to Fe²⁺. We surmise that nonstoichiometric charge storage of 95 additional electrons arises from multielectron reduction of either Zn²⁺ or Fe³⁺. Such additional reduction would be consistent with evidence of partial Zn²⁺ reduction to Zn(0) in ZnO NCs when photodoped in the presence of excess Li⁺.

$$K_{\text{eq}} = [e^{-}_{\text{CB}}][\text{Fe}^{3+}]/[\text{Fe}^{2+}]$$
 (2)

$$\Delta E = (RT/nF)\log K_{\rm eq} \tag{3}$$

Potentiometric titration provides independent confirmation of enhanced charge-storage capacity in these colloidal Zn_{0.99}Fe_{0.01}O NCs and yields a quantitative measure of the NC capacitance itself. Figure 2A plots open-circuit potentials

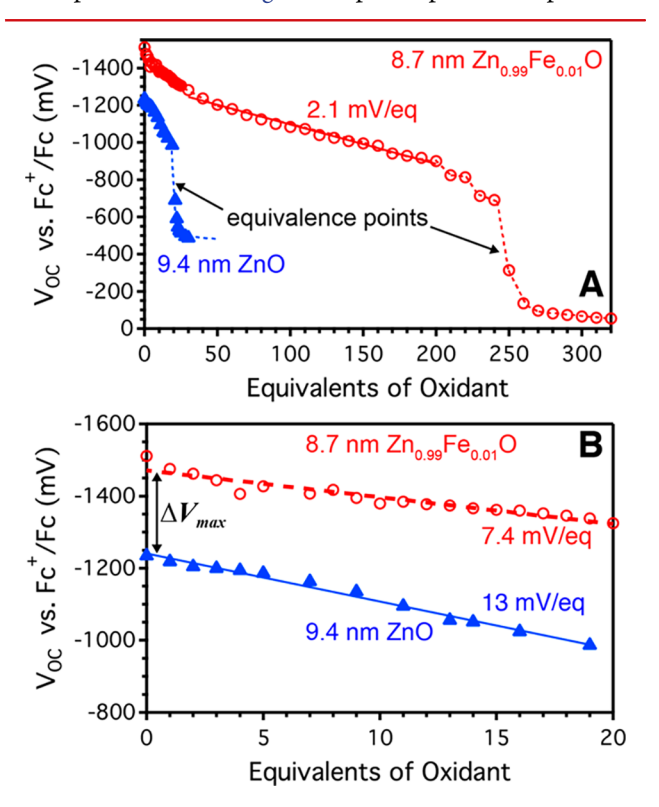


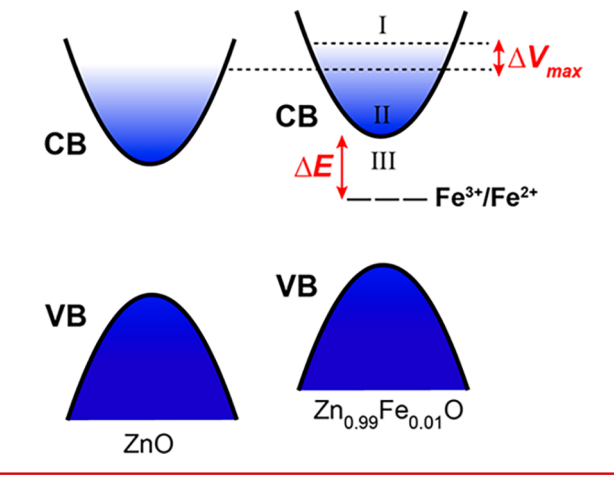
Figure 2. Comparison of potentiometric titration data for undoped and Fe-doped ZnO NCs. (A) Red: Titration data for d=8.7 nm Zn_{0.99}Fe_{0.01}O NCs. The solid line shows the linear best fit of the data from 20–200 equiv and has a slope of 2.1 mV/equiv. Solutions contained 0.4 μM NC in THF with 0.1 M TBAPF₆ as supporting electrolyte, and titration was performed using FcBF₄. Blue: Titration data for d=9.4 ZnO NCs, adapted from ref 12. Titration was performed using [Fc*][BArF₄]. The difference between red and blue potentials after removal of all electrons simply reflects the difference between FcBF₄ and [Fc*][BArF₄] reduction potentials. (B) Expanded view of the data from panel A between 0 and 20 equiv of added oxidant. Best-fit lines through the Zn_{0.99}Fe_{0.01}O and ZnO NC data are shown as dashed red and solid blue lines, with slopes of 7.4 and 13 mV/equiv, respectively. $\Delta V_{\rm max}$ denotes the difference in $V_{\rm OC}$ between the two curves at maximal photodoping (zero oxidant).

 $(V_{\rm OC})$ vs added equivalents of oxidant measured for these photodoped $\rm Zn_{0.99}\rm Fe_{0.01}\rm O$ NCs. For comparison, analogous data for ZnO NCs of a similar size are also plotted. 12 $V_{\rm OC}$ measures the Fermi level of the colloidal suspension, interchangeably called the redox potential. For clarity, the data between 0 and 20 oxidizing equivalents are replotted on an expanded scale in Figure 2B. Several key differences between the $\rm Zn_{0.99}\rm Fe_{0.01}\rm O$ and ZnO NCs are apparent from these data. First, as determined from the data in Figure 1, many more reducing equivalents are stored in the $\rm Zn_{0.99}\rm Fe_{0.01}\rm O$ NCs than in ZnO NCs. Whereas these ZnO NCs require 20 equiv to reach the equivalence point (the potential at which $\langle n\rangle$ = 0 and no excess oxidant is present), the $\rm Zn_{0.99}\rm Fe_{0.01}\rm O$ NCs require 250 equiv.

In contrast with the three distinct titration regimes observed spectroscopically (Figure 1C) for the Zn_{0.99}Fe_{0.01}O NCs, only two regimes are apparent in the potentiometric titration data of Figure 2A. The first extends from 0-20 equiv, encompassing both Regimes I and II of Figure 1C. Data in this range are fit well with a single slope of 7.4 mV/equiv. There is thus no distinct manifestation of the transition from Regime I to Regime II in these potentiometric titration data. The absence of a pronounced step in this range is consistent with the presence of a redox equilibrium between the CB edge and Fe(3d) orbitals. Pronounced steps in potentiometric titration curves are only observed when redox potentials differ by \gtrsim 180 mV.²⁰ From 20-200 equiv, the potentiometric data are fit to a shallower slope of 2.1 mV/equiv. This slope is interpreted as reflecting oxidation of an ensemble of Fe2+ dopants at nearly one single redox potential (vide infra).

Scheme 1 summarizes the electronic structure of these $Zn_{1-x}Fe_xO$ NCs and its relationship to that of ZnO NCs

Scheme 1. Relevant Electronic Structure Differences between Zn_{1-x}Fe_xO and ZnO NCs Deduced from Potentiometric Titration Measurements



deduced from these data. The most distinctive feature of these $Zn_{0.99}Fe_{0.01}O$ NCs is that they possess a set of redox-active midgap Fe(3d) orbitals situated $\Delta E\approx 136$ mV below the CB edge. The first added electrons fill these localized orbitals, and subsequent added electrons fill the CB. The highly localized nature of the Fe(3d) orbitals allows a large number of excess noninteracting electrons to be stored within a single $Zn_{1-x}Fe_xO$ NC at almost the same potential, lending these NCs very large redox capacitances. Despite being largely localized, these Fe(3d) electrons are still easily removed, even by solvated

outer-sphere oxidants, because they are in equilibrium with the CB. The three regimes identified by optical titration (I, II, and III) are indicated in Scheme 1, and correspond to (I) removal of \sim 1 CB electron per oxidizing equivalent, (II) removal of <1 CB electron per oxidizing equivalent because of refilling by Fe²⁺ ionization to the CB, and (III) removal of \sim 1 Fe(3d) electron per oxidizing equivalent. The experimental data also show more negative potentials for the Zn_{0.99}Fe_{0.01}O NCs, illustrated here by $\Delta V_{\rm max}$ and the CB-edge offset relative to the ZnO NCs.

The value of $\langle n_{\text{max}}(\text{CB}) \rangle \approx 5$ for these $\text{Zn}_{0.99}\text{Fe}_{0.01}\text{O}$ NCs corresponds to a charge carrier density of only $\sim 1.4 \times 10^{19}$ cm⁻³, which is 10 times smaller than observed for comparable ZnO NCs of the same diameter photodoped by the same method. The data in Figure 2 also show that the potentials of the photodoped Zn_{0.99}Fe_{0.01}O NCs are significantly more negative than those of the ZnO NCs, with $\Delta V_{\rm max} \approx -300$ mV. In colloidal CdSe NCs, surface dipoles were found to destabilize the NC band edges, causing both more negative band-edge potentials and the accumulation of fewer CB electrons during photodoping. 10,21 Similarly, we hypothesize that the 95 additional electrons identified by potentiometric and optical titration act as localized lattice anions that destabilize additional CB electrons. This Coulombic interaction can be assessed using the "charged sphere" model. 5,22 Assuming a uniform distribution of the additional localized electrons within the NC interior, the charged sphere model predicts a ΔV_{max} of -270 mV for these $Zn_{0.99}Fe_{0.01}O$ NCs, with each localized charge contributing -2.84 mV on average (details provided in the Supporting Information). For comparison with the experimental data in Figure 2B, Figure 3 plots simulated

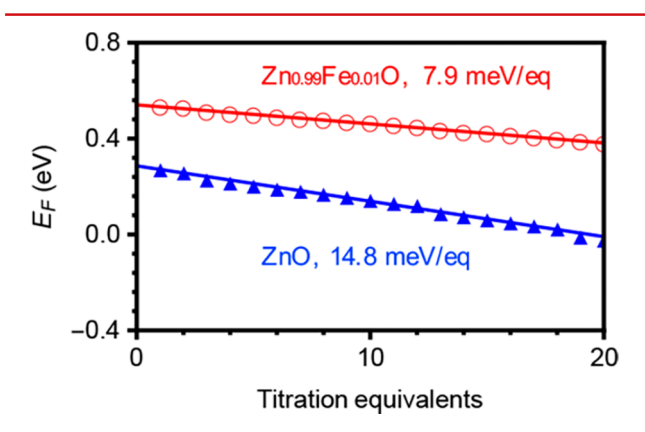


Figure 3. Calculated potentiometric titration curves. Simulated potentiometric titrations of photodoped d=8.7 nm $\mathrm{Zn_{0.99}Fe_{0.01}O}$ and ZnO NCs (with and without additional localized electrons, respectively), calculated using the "charged sphere" model.^{5,22} For convenience, both calculations use $n_{\mathrm{max}}(\mathrm{CB})=20$. The zero reference energy $(E_{\mathrm{F}}=0)$ is set as $1/\varepsilon_{\mathrm{R}}R$ over the CB edge of the ZnO NCs, i.e., $V(n=0)=V(20\ \mathrm{equiv})=-1/\varepsilon_{\mathrm{R}}R$.

potentiometric titration data from this model for d=8.7 nm $Zn_{0.99}Fe_{0.01}O$ and ZnO NCs. For convenience, the calculations use $n_{\rm max}({\rm CB})=20$ in each case, but this number does not influence the results. Figure 3 shows that the charged sphere model predicts a shallower titration slope for the $Zn_{0.99}Fe_{0.01}O$ NCs than for the ZnO NCs, precisely as observed experimentally. The calculations also predict $\Delta V_{\rm max}<0$ and on the same order of magnitude as observed experimentally. The titration slope is shallower because, compared with undoped ZnO, titration of photodoped $Zn_{0.99}Fe_{0.01}O$ is less

effective at reducing interelectronic repulsion: the first several equivalents of oxidant added to maximally photodoped $\mathrm{Zn_{1-x}Fe_xO}$ NCs remove only CB electrons, which eliminates interelectronic repulsion between CB electrons but not the destabilizing influence of the deeper localized electrons. From these calculations, we conclude that the additional localized electrons deduced from the titration data are also responsible for both ΔV_{max} and the difference in slopes in the experimental potentiometric titration data of the $\mathrm{Zn_{0.99}Fe_{0.01}O}$ and ZnO NCs shown in Figure 2.

Finally, the experimental $V_{\rm OC}$ data in Figure 2 allow quantitative analysis of the capacitance of these NCs. As described previously, 12 the charge-storage ability of colloidal NCs, termed the redox capacitance (C_r) , is inversely related to the slope of the NC's potentiometric titration curve. A steep slope corresponds to a small C_r. Classical double-layer capacitance (C_{dl}) and quantum capacitance (C_{Q}) contribute in series to C_r . C_Q is defined by $C_Q = e(dQ/d\mu) = e^2g(E)$, where e is the elementary charge, g(E) is the density of states at energy E, and $dQ/d\mu$ is the change in charge per unit change in electrochemical potential.^{23,24} From Figure 2, the shallower slope between 0-20 equiv observed for the Zn_{0.99}Fe_{0.01}O NCs compared to the ZnO NCs indicates enhanced NC capacitance, and its numerical value (7.4 mV/equiv) indicates $C_r = 47$ aF. The smaller slope of 2.1 mV/equiv seen between 20-200 equiv reflects an even larger value of $C_{\rm r}$ = 80 aF. These large capacitance values reflect how small changes in the solution Fermi level cause large changes in the number of stored electrons. Microscopically, these high capacitance values are attributable to the redox activity of the Fe(3d) midgap orbitals, which collectively offer a high density of states with negligible dispersion.

Remarkably, the charge-storage capabilities of these colloidal $Zn_{0.99}Fe_{0.01}O$ NCs rival those found in conventional electrical double-layer supercapacitor devices. The areal capacitance of 33 μ F cm⁻² found here exceeds typical values for activated carbon, $^{25-27}$ as well as for state-of-the-art electrodes based on metal—organic frameworks²⁸ and holey graphene, 29 all of which fall around 5 to 15 μ F cm⁻². Normalized for NC volume, the volumetric capacitance of 233 F cm⁻³ observed here also surpasses any commercial carbon-based material reported to date. Neglecting surface ligands, which could be stripped from the $Zn_{1-x}Fe_xO$ NCs, these values correspond to a high gravimetric capacitance of 50 F g⁻¹. Because C_r scales with dopant concentration (x), these colloidal $Zn_{1-x}Fe_xO$ NCs also offer synthetically accessible routes for increasing or optimizing their supercapacitance.

In addition to serving as soluble supercapacitors for various flow-type charge-storage technologies or as reversible multielectron reductants for redox catalysis, colloidal Zn_{1-x}Fe_xO NCs may also be attractive as simple precursors for capacitor electrodes. To explore this concept, we prepared electrodes functionalized with ~100 μ g of Zn_{0.99}Fe_{0.01}O or ZnO NCs by simple drop-casting of the colloidal NCs onto FTO-coated glass (1.0 \times 0.5 cm), followed by ligand removal, all at room temperature (see Supporting Information). Figure 4 shows cyclic voltammograms collected using these as the working electrodes. Currents are presented as specific capacitances. A quasi-reversible feature at ~-700 mV is tentatively assigned to pseudocapacitive charging of Fe dopants near the NC surfaces. With no optimization, these data already show greatly enhanced capacitance in the Zn_{0.99}Fe_{0.01}O film relative to the ZnO film. Integration of these data yields average gravimetric

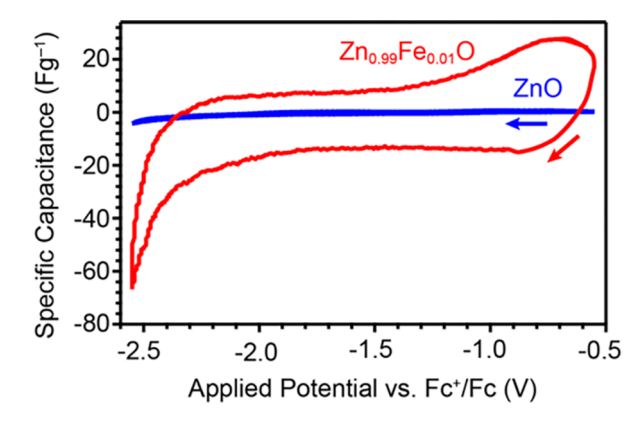


Figure 4. Capacitor electrodes made from colloidal NCs. Cyclic voltammograms of drop-cast $Zn_{0.99}Fe_{0.01}O$ (red) and ZnO (blue) NCs on FTO measured in a three-electrode cell. Data were collected at a scan rate of 10 mV s⁻¹, from a rest $V_{\rm OC} = -0.55$ V, and were initially swept cathodically, as indicated by the arrows. Specific capacitance values represent the current divided by the scan rate.

capacitances of 12 F g⁻¹ for the Zn_{0.99}Fe_{0.01}O film compared to just 0.4 F g⁻¹ for the ZnO film. Although these gravimetric capacitances are lower than in pseudocapacitors such as NiO or RuO₂, it may be possible to achieve gravimetric capacitances comparable to commercial supercapacitors based on activated carbon²¹ (\sim 100 F g⁻¹) by increasing the Fe doping level or optimizing the electrode fabrication. Overall, these data represent a proof-of-concept demonstration that these soluble supercapacitors can be used to prepare wired capacitors suitable for applications such as photoelectrochemical energy storage.³⁰

In summary, potentiometric titration measurements reveal very large capacitances in free-standing colloidal Zn_{0.99}Fe_{0.01}O NCs, attributable to the presence of midgap Fe(3d) orbitals that can reversibly capture and store added electrons. The Fe³⁺electron binding energy of ~136 meV is sufficiently large for these electrons to be localized in the form of Fe²⁺ dopants, but it is simultaneously sufficiently small that these electrons remain in equilibrium with the ZnO NC CB and consequently can still be easily removed by outer-sphere oxidants in solution. These features make Zn_{0.99}Fe_{0.01}O NCs attractive candidates for high-capacitance charge-storage applications. In addition to these properties, potentiometric titration measurements demonstrate that the band edges of the Zn_{0.99}Fe_{0.01}O NCs are destabilized by ~300 mV relative to those of analogous ZnO NCs. Analysis of this result within the charged sphere model suggests that these band-edge potentials are destabilized because of new repulsive Coulombic interactions involving CB electrons and electrons localized in midgap orbitals that are not present in analogous ZnO NCs. Overall, these results reveal colloidal Zn_{1-x}Fe_xO NCs, and doped semiconductor nanocrystals more generally, as attractive "soluble supercapacitors" that are well suited for use in solution-phase charge-storage or multielectron redox processes and that are also amenable to processing for preparation of electrochemical energy-storage electrodes.

ASSOCIATED CONTENT

S Supporting Information

The Supporting Information is available free of charge on the ACS Publications website at DOI: 10.1021/acs.nanolett.8b01264.

Detailed descriptions of experimental methods, description of charged sphere calculations, and nanocrystal XRD and TEM data (PDF)

AUTHOR INFORMATION

Corresponding Author

*E-mail: gamelin@chem.washington.edu.

ORCID ®

Carl K. Brozek: 0000-0002-8014-7904 Hongbin Liu: 0000-0001-9011-1182 Xiaosong Li: 0000-0001-7341-6240 Kevin R. Kittilstved: 0000-0002-9852-7454 Daniel R. Gamelin: 0000-0003-2888-9916

Notes

The authors declare no competing financial interest.

ACKNOWLEDGMENTS

This research was partially supported by the U.S. National Science Foundation through the University of Washington Molecular Engineering Materials Center, a Materials Research Science and Engineering Center (DMR-1719797). Additional financial support from the U.S. National Science Foundation (CHE-1506014 to D.R.G.; CHE-1454930 to K.R.K.; CHE-1565520 to X.L.) is gratefully acknowledged. The authors thank Dr. Danielle Henckel for guidance in preparing capacitor electrodes. This research was supported in part by the State of Washington through the University of Washington Clean Energy Institute through the Washington Research Foundation (to C.K.B.).

■ REFERENCES

- (1) Schimpf, A. M.; Thakkar, N.; Gunthardt, C. E.; Masiello, D. J.; Gamelin, D. R. ACS Nano 2014, 8, 1065–1072.
- (2) Jain, P. K.; Manthiram, K.; Engel, J. H.; White, S. L.; Faucheaux, J. A.; Alivisatos, A. P. *Angew. Chem., Int. Ed.* **2013**, *52*, 13671–13675.
- (3) Llordes, A.; Wang, Y.; Fernandez-Martinez, A.; Xiao, P.; Lee, T.; Poulain, A.; Zandi, O.; Saez Cabezas, C. A.; Henkelman, G.; Milliron, D. J. Nat. Mater. 2016, 15, 1267–1273.
- (4) Knowles, K. E.; Malicki, M.; Weiss, E. A. J. Am. Chem. Soc. 2012, 134, 12470–12473.
- (5) Liu, H.; Brozek, C. K.; Sun, S.; Lingerfelt, D. B.; Gamelin, D. R.; Li, X. J. Phys. Chem. C 2017, 121, 26086–26095.
- (6) Wu, K.; Rodriguez-Cordoba, W. E.; Yang, Y.; Lian, T. Nano Lett. **2013**, 13, 5255–5263.
- (7) Wood, A.; Giersig, M.; Mulvaney, P. J. Phys. Chem. B 2001, 105, 8810–8815.
- (8) Haase, M.; Weller, H.; Henglein, A. J. Phys. Chem. 1988, 92, 482–487.
- (9) Schimpf, A. M.; Gunthardt, C. E.; Rinehart, J. D.; Mayer, J. M.; Gamelin, D. R. J. Am. Chem. Soc. 2013, 135, 16569–16577.
- (10) Carroll, G. M.; Brozek, C. K.; Hartstein, K. H.; Tsui, E. Y.; Gamelin, D. R. J. Am. Chem. Soc. 2016, 138, 4310–4313.
- (11) Carroll, G. M.; Tsui, E. Y.; Brozek, C. K.; Gamelin, D. R. Chem. Mater. 2016, 28, 7912–7918.
- (12) Brozek, C. K.; Hartstein, K. H.; Gamelin, D. R. J. Am. Chem. Soc. **2016**, 138, 10605–10610.
- (13) Hartstein, K. H.; Brozek, C. K.; Hinterding, S. O. M.; Gamelin, D. R. J. Am. Chem. Soc. **2018**, 140, 3434–3442.
- (14) Zhou, D.; Kittilstved, K. R. J. Mater. Chem. C 2015, 3, 4352-4358.
- (15) Zhou, D.; Kittilstved, K. R. Chem. Commun. 2016, 52, 9101–9104.
- (16) Liu, W. K.; Whitaker, K. M.; Kittilstved, K. R.; Gamelin, D. R. J. Am. Chem. Soc. **2006**, 128, 3910–3911.

(17) Ochsenbein, S. T.; Feng, Y.; Whitaker, K. M.; Badaeva, E.; Liu, W. K.; Li, X.; Gamelin, D. R. *Nat. Nanotechnol.* **2009**, *4*, 681–687.

- (18) Cohn, A. W.; Kittilstved, K. R.; Gamelin, D. R. J. Am. Chem. Soc. **2012**, 134, 7937–7943.
- (19) Quemener, V.; Vines, L.; Monakhov, E. V.; Svensson, B. G. Appl. Phys. Lett. 2013, 102, 232102.
- (20) Kolthoff, I. M.; Furman, N. H. Potentiometric Titrations, a Theoretical and Practical Treatise, 2nd ed.; J. Wiley and Sons, 1931.
- (21) Carroll, G. M.; Schimpf, A. M.; Tsui, E. Y.; Gamelin, D. R. *J. Am. Chem. Soc.* **2015**, *137*, 11163–11169.
- (22) We used a modified version of the charge sphere model from ref 5. A detailed description will be presented in a forthcoming publication, but a brief synopsis is provided in the Supporting Information.
- (23) Iafrate, G. J.; Hess, K.; Krieger, J. B.; Macucci, M. Phys. Rev. B: Condens. Matter Mater. Phys. 1995, 52, 10737–10739.
- (24) Büttiker, M.; Thomas, H.; Prêtre, A. Phys. Lett. A 1993, 180, 364-369.
- (25) Burke, A. Electrochim. Acta 2007, 53, 1083-1091.
- (26) Chmiola, J.; Yushin, G.; Gogotsi, Y.; Portet, C.; Simon, P.; Taberna, P. L. Science **2006**, 313, 1760–1763.
- (27) Centeno, T. A.; Stoeckli, F. Electrochim. Acta 2011, 56, 7334-7339.
- (28) Sheberla, D.; Bachman, J. C.; Elias, J. S.; Sun, C. J.; Shao-Horn, Y.; Dinca, M. *Nat. Mater.* **2017**, *16*, 220–224.
- (29) Xu, Y.; Lin, Z.; Zhong, X.; Huang, X.; Weiss, N. O.; Huang, Y.; Duan, X. Nat. Commun. 2014, 5, 4554.
- (30) Miyasaka, T.; Murakami, T. N. Appl. Phys. Lett. **2004**, 85, 3932—3934.